ANNALS OF PHYSICS 209, 327–363 (1991)

Pair Correlations near the Neutron Drip Line

G. F. BERTSCH

Cyclotron Laboratory, Michigan State University, East Lansing, Michigan 48824

AND

H. ESBENSEN

Physics Division, Argonne National Laboratory, Argonne, Illinois 60439

Received October 11, 1990; revised January 23, 1991

A theory of pairing in weakly bound nuclei is presented. The nucleus is treated as a three-body system consisting of two interacting nucleons together with a structureless core. The pairing interaction is modelled by a density-dependent contact interaction. It is constrained to the free nucleon interaction at low density. Numerically, the Hamiltonian equation is solved by a two-particle Green's function method in coordinate space. Given the single particle resonance energy of ^{10}Li, the theory reproduces the marginal binding of ^{11}Li. The large electric dipole stength in ^{11}Li found experimentally is also accounted for. The nucleus ^{14}Be is also found to be bound.

CONTENTS

1. INTRODUCTION

It is now feasible to study nuclei on the very edge of particle stability at the neutron drip line. Such nucei are expected to have quite different properties from ordinary nuclei, due to the weakly bound neutrons which extend well beyond the nuclear surface.

The U.S. Government's right to retain a nonexclusive royalty-free license in and to the copyright covering this paper, for governmental purposes, is acknowledged.

0003-4916/91 $7.50

In principle, the theory of drip line nuclei is just an extension of the shell model to a domain of very weakly bound states. This straightforward approach has been taken by Hoshino *et al.* [1]. However, several problems arise in making a realistic description. First of all, the shell model orbitals no longer provide a good starting point when the residual interaction is neglected—the valence particles may not even be bound in the absence of that interaction. Another problem is treating the interaction in the nuclear exterior. Here the many-body effects are small and the interaction should be close to the free-particle interaction. Of course, excellent models are available for the free interaction, but they all require accurate modelling of the wave function at short distances, due to the strong correlations.

It is hardly practical to make a calculation that simultaneously deals with these two problems, the accurate descriptions of the single-particle wave function at large distances and the relative wave function of valence particles at short distances. We shall avoid the relative wave function problem in the usual way, replacing the realistic interaction by an effective interaction. The large single-particle space can be handled using a Green's function technique, provided the effective interaction is a contact interaction. We shall therefore use a residual interaction of that form, i.e., a delta-function in the relative coordinate.

It requires some care to specify the interaction, and this task makes up a considerable part of the present work. A delta-function interaction only has meaning in a truncated space, so we shall need to know the working space before the interaction can be defined. The physical criterion defining the interaction in the far exterior is that it produces a large scattering length. We will find that an effective interaction defined this way is too strong in the nuclear interior. We shall therefore give it a phenomenological density dependence that describes pairing in more tightly bound nuclei.

The theory will then predict the binding energy and the ground state wave function, given the single-particle Hamiltonian. With this information one can calculate density distributions, which in turn can be applied to reaction cross sections at high energy. An interesting property of these nuclei is an enhanced dipole stength function at low excitation. Some integrated properties of this can be calculated from the ground state density. The detailed stength distribution is more difficult to calculate, but we have a good idea of its qualitative behavior from the independent particle model.

This will all be applied to the nucleus ^{11}Li, which has been studied in a number of experiments. We shall find that the theoretical pairing successfully explains the existence of this bound nucleus, despite the fact that the valence orbital is unbound by 0.8 MeV. The large reaction cross sections and dipole excitation cross sections are also qualitatively accounted for in the theory.

2. Effective Interaction

Our calculations of the two-neutron wave function are based on the two-particle Green's function method which is discussed in the next section. The method is more

efficient than the usual Hamiltonian diagonalization when a zero-range form is used for the nucleon–nucleon interaction. Zero-range interactions lead to divergencies and can only be meaningful as effective interactions within a truncated space of states. We shall impose a cutoff in the two-particle energy spectrum, as is usually done in pairing calculations, to make the truncation. The parameters of the interaction are then adjusted so that observables are reproduced. We choose the following parameterization of the effective interaction:

$$v_{\text{eff}}(\mathbf{r}_1, \mathbf{r}_2) = \delta(\mathbf{r}_1 - \mathbf{r}_2)\left(v_0 + v_\rho\left(\frac{\rho_c((\mathbf{r}_1 + \mathbf{r}_2)/2)}{\rho_0}\right)^P\right). \tag{2.1}$$

We first determine the density independent term v_0 to simulate the interaction between free neutrons. The density dependent term contains the ratio of the nuclear core density, $\rho_c(r)$, and nuclear matter density, $\rho_0 = 0.16\ \text{fm}^{-3}$. We shall later adjust the strength v_ρ and the power P so that the pairing enegies in p-shell nuclei are reasonably well repreduced (see Section 4).

Let us first discuss the correlation between free neutrons. The wave function for the relative motion, with reduced mass $m/2$, is then determined by

$$\left(-\frac{\hbar^2}{m}\nabla^2 + v_0\,\delta(\mathbf{r})\right)\psi(\mathbf{r}) = E\psi(\mathbf{r}). \tag{2.2}$$

The formal solution to this equation is

$$\psi(\mathbf{r}) = \psi^{(0)}(\mathbf{r}) - \int d\mathbf{r}'\, G_0(\mathbf{r}, \mathbf{r}', E)\, v_0\, \delta(\mathbf{r}')\, \psi(\mathbf{r}'), \tag{2.3}$$

where $\psi^{(0)}$ is a solution of the homogeneous equation (i.e. without the interaction) and G_0 is the free Greens function in the truncated space, $\varepsilon_k \leqslant E_c$ or $k \leqslant k_c$,

$$G_0(\mathbf{r}, \mathbf{r}', E) = \frac{1}{(2\pi)^3}\int_{\varepsilon_k \leqslant E_c} d\mathbf{k}\, \frac{e^{i\mathbf{k}(\mathbf{r}-\mathbf{r}')}}{\varepsilon_k - E}. \tag{2.4}$$

In order to simulate the fact that the scattering length for free neutrons is very large we require that Eq. (2.3) have a bound state solution at zero energy. This implies that $\psi^{(0)} = 0$ and leads to the condition at $\mathbf{r} = 0$,

$$1 = -\frac{v_0}{(2\pi)^3}\int_{\varepsilon_k \leqslant E_c} d\mathbf{k}\, \frac{1}{\varepsilon_k}. \tag{2.5}$$

The integration over $\mathbf{k}$ is trivial and leads to an expression for the interaction strength in terms of the cutoff energy,

$$v_0 = -2\pi^2\left(\frac{\hbar^2}{m}\right)^{3/2} E_c^{-1/2}. \tag{2.6}$$

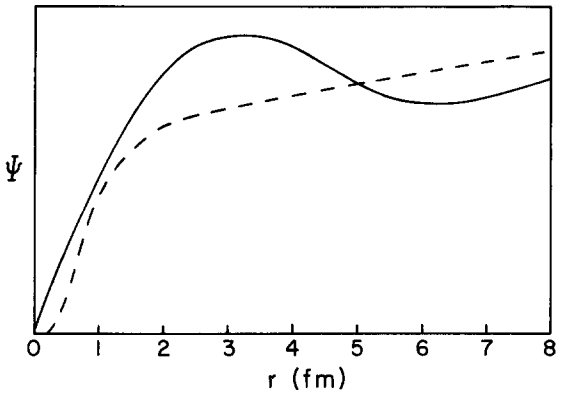

FIG. 1. Radial wave functions for the relative motion of two neutrons. The fully drawn curve is the sine-integral function $Si(k_c r)$, obtained from the local pairing interaction Eq. (2.6), which produces a bound state at zero energy. The dashed curve is the result obtained from the Reid soft-core potential.

We have chosen the cutoff energy $E_c = 40$ MeV for all of our calculations, with the corresponding interaction stength $v_0 = -831$ MeV fm^3.

It is also interesting to study the bound state wave function at zero energy. It is given by Eqs. (2.3)–(2.4), and substituting the expression (2.6) for the strength v_0 we obtain

$$\psi(\mathbf{r}) = \psi(0)\, Si(k_c r)/(k_c r), \tag{2.7}$$

where $Si(x)$ is the sine integral function, $Si(x) = \int_0^x dt \sin(t)/t$. The radial wave function is proportional to $Si(k_c r)$, which is illustrated in Fig. 1, together with the radial wave function obtained from a commonly used finite range interaction, namely, the Reid soft core potential [2].

3. Calculational Technique

The problem we want to study is the effect of pairing between two valence nucleons outside an inert core. Thus we need to find the eigenstates of a two-particle Hamiltonian of the form

$$H_2(\mathbf{r}_1, \mathbf{r}_2) = H_2^{(0)}(\mathbf{r}_1, \mathbf{r}_2) + v_{\text{eff}}(\mathbf{r}_1, \mathbf{r}_2), \tag{3.1}$$

where $H_2^{(0)} = H_1(\mathbf{r}_1) + H_1(\mathbf{r}_2)$ is the sum of the single-particle shell model Hamiltonians for the two valence nucleons, and v_{eff} is the pairing interaction (2.1). The kinetic energy associated with the core motion is neglected. We take as our single-particle basis the eigenstates of H_1, which is an ordinary single-particle Hamiltonian consisting of a kinetic energy operator, a Woods–Saxon potential and

a spin-orbit interaction. This space includes bound states as well as continuum states, but bound states occupied by the core nucleons are explicitly excluded from the space. Thus we effectively solve the Bethe–Goldstone equation for the two valence neutrons in the presence of the core. The continuum is discretized by putting the wave functions in a spherical box, requiring the wave functions to vanish at the boundary.

The most straightforward way to find the eigenfunctions and energies of the two-particle Hamiltonian (3.1) is to diagonalize the Hamiltonian matrix. First we set up a two-particle shell model basis, $|2p\rangle = |p_1, p_2\rangle$, using the single-particle wavefunctions discussed above. An integral part of our model is the cutoff in the two-particle energy spectrum, E_c, which has to be chosen consistently with the pairing interaction at zero density, cf. Section 2, Eq. (2.6). The quantum numbers of the ground state, positive parity and total angular momentum zero, also reduce the number of states that need to be included. Of course, nuclei such as ^{11}Li have non-zero ground state spins, but our model ignores the internal structure of the core.

Since the pairing interaction is assumed to be of zero range, we shall only need the two-particle shell model wave functions at $\mathbf{r}_1 = \mathbf{r}_2$. Expressions for the wave functions and the needed amplitudes are given in Appendix A. To proceed with the Hamiltonian diagonalization, the matrix elements of the pairing interaction are calculated. The full Hamiltonian matrix, given in Eq. (B.1) of Appendix B, is then diagonalized. We shall find that numerical convergence for ^{11}Li is only reached with matrices in spaces of several thousand two-particle states. Once the ground state energy and the amplitudes of the ground state on the independent two-particle states have been determined, the ground state wave function and density can be calculated as described in Appendix B. The ground state density we obtain for ^{11}Li is discussed in Section 5.

For most of our calculations we have actually used a more efficient method based on the two-particle Green's function. This only requires matrices of dimensionality of the order of 100 to achieve numerical convergence. Since this method has not been commonly used as a numerical technique in nuclear physics, we shall describe it in some detail.

3.1. *Green's Function Method*

We first define the independent two-particle Green's function as

$$G_2^{(0)}(E) = (H_2^{(0)} - E - i\eta)^{-1} = \sum_{2p} \frac{|2p\rangle\langle 2p|}{\varepsilon_{2p}^{(0)} - E - i\eta}. \tag{3.2}$$

It is an operator in the space of two-particle states $|2p\rangle$ with energies $\varepsilon_{2p}^{(0)}$. The correlated two-particle Green's function is defined in a similar way,

$$G_2(E) = (H_2 - E - i\eta)^{-1} = \sum_{\widetilde{2p}} \frac{|\widetilde{2p}\rangle\langle\widetilde{2p}|}{\varepsilon_{2p} - E - i\eta}, \tag{3.3}$$

where $|\widetilde{2p}\rangle$ are the correlated two-particle states, which are the eigenfunctions to the total Hamiltonian H_2 that we want to determine, with eigenvalues ε_{2p}. These Green's functions are fairly complicated since they depend on four positions $(\mathbf{r}_1, \mathbf{r}_2, \mathbf{r}_1', \mathbf{r}_2')$ in coordinate space. However, the calculation of the correlated two-particle states can be simplified considerably by exploiting the fact that the pairing interaction is assumed to be of zero range. To see this let us first note the relations

$$1 + G_2^{(0)}(E)\, v_{\text{eff}} = G_2^{(0)}(E)(H_2^{(0)} + v_{\text{eff}} - E - i\eta) = G_2^{(0)}(E)\, G_2(E)^{-1}. \tag{3.4}$$

From this expression we can isolate the correlated Green's function

$$G_2(E) = (1 + G_2^{(0)}(E)\, v_{\text{eff}})^{-1} G_2^{(0)}(E). \tag{3.5}$$

It is now convenient to multiply the operator $G_2(E)$ by $\delta(\mathbf{r}_1 - \mathbf{r}_2)$. Taking matrix elements of the resulting operator between two independent two-particle states we obtain, using (3.2) and (3.3),

$$\langle 2p_0|\, \delta(\mathbf{r}_1 - \mathbf{r}_2)\, G_2(E)\, |2p\rangle = \sum_{\widetilde{2p}} \frac{\langle 2p_0|\, \delta(\mathbf{r}_1 - \mathbf{r}_2)\, |\widetilde{2p}\rangle \langle \widetilde{2p}\, |\, 2p\rangle}{\varepsilon_{2p} - E - i\eta} \tag{3.6a}$$

$$= \frac{\langle 2p_0|\, \delta(\mathbf{r}_1 - \mathbf{r}_2)(1 + G_2^{(0)}(E)\, v_{\text{eff}})^{-1}\, |2p\rangle}{\varepsilon_{2p}^{(0)} - E - i\eta}. \tag{3.6b}$$

These relations solves the problem at hand. Equation (3.6a) shows that the expression diverges when E is identical to one of the correlated energy eigenvalues. Alternatively, keeping a finite (but small) imaginary part $i\eta$, the imaginary part of this expression will have a local maximum when E coincides with an eigenvalue. A simple search can therefore be made to locate the ground state energy of the pair. The amplitudes of the ground state wave function on two-particle shell model states can also be extracted. Equations (3.6a)–(3.6b) show that

$$\langle \widetilde{2p}\, |\, 2p\rangle = N \operatorname{Im} \frac{\langle 2p_0|\, \delta(\mathbf{r}_1 - \mathbf{r}_2)(1 + G_2^{(0)}(E)\, v_{\text{eff}})^{-1}\, |2p\rangle}{\varepsilon_{2p}^{(0)} - E - i\eta}, \tag{3.7}$$

when E is set equal to the ground state energy of the pair. Here N is a constant that can be eliminated by the normalization of the ground state wave function. The state $|2p_0\rangle$ is fixed in this process but it can otherwise be any of the two-particle states. We note that we shall determine the amplitudes from the imaginary part of the matrix elements, Eq. (3.7), with a non-zero $i\eta$. To obtain them from the real part, with $\eta = 0$, would probably be uncertain since the expression diverges at the energy eigenvalue.

The derivation given above is formal and needs further specifications in order to apply it in practice. The local independent two-particle Green's function can be constructed from the two-particle states given in Appendix A. The ground state of

the pair is a $J=0$ state, and the associated part of the Green's function is (cf. Eq. (A.7)),

$$G_2^{(0)}(r, r', E) = \sum_{nn'lj} \frac{\phi_{nlj}(r)\,\phi_{n'lj}(r)\,\phi_{nlj}(r')\,\phi_{n'lj}(r')}{\varepsilon_{nlj}+\varepsilon_{n'lj}-E-i\eta} \frac{2j+1}{8\pi} Y_{00}(\hat{r})\,Y_{00}(\hat{r}'). \quad (3.8)$$

This is the local two-particle Green's function for $J=0$. We have dropped the spin-dependence contained in (A.6), since it is a simple $S=0$ state. Thus the ground state energy of the pair depends only on the $S=0$ component of the two-particle wave functions. The ground state wave function does contain an $S=1$ component, but it vanishes at $\mathbf{r}_1=\mathbf{r}_2$.

The main complication in the numerical calculation of (3.7) is the inversion of the operator $1+G_2^{(0)}(E)v_{\text{eff}}$. This inversion is similar to the one used in ordinary RPA theory [3], and it can be performed on a finite radial grid. The size of this matrix is much smaller than the dimension of the Hamiltonian matrix (B.1). The approach based on the two-particle Green's function may therefore be much faster. This is actually the case for the calculations presented in Sections 4 and 5.

3.2. *Numerical Tests*

It is very important to be able to test the numerical calculations based on the two-particle Green's function method. Here we shall mention three tests that we

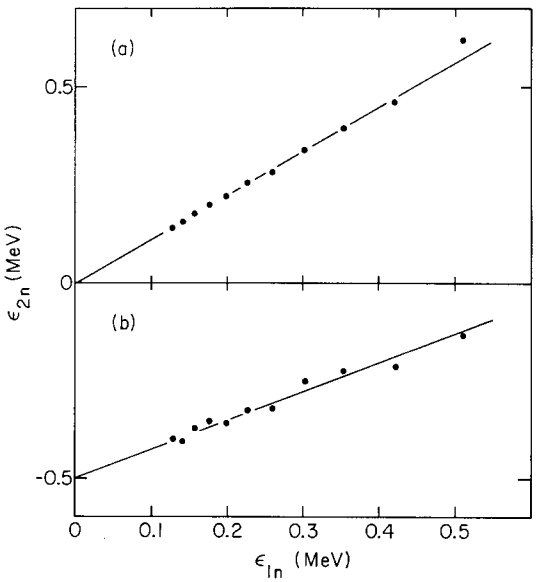

FIG. 2. Correlated two-neutron energy as a function of the smallest energy of the one-neutron states included. The calculations (dots) have been performed for free neutrons, with the local pairing interaction (3.9) adjusted to produce a bound state at zero (a) and at -0.5 MeV (b), respectively. The smallest one-neutron energy was varied by changing the radial cutoff, from 20 to 40 fm.

have made use of. First of all, one can compare to the results of the Hamiltonian diagonalization method already mentioned. We have found that the two methods give almost identical results for the ground state energy and also for the ground state density (within a few percent) when the value of η is chosen sufficiently small (say $\eta = 0.01$ MeV). The two methods must, of course, give identical results in the limit where η goes to zero.

Another test of the Green's function method can be made by assuming that the single-particle potential is a harmonic oscillator potential (without spin-orbit), and that the pairing interaction is a density independent contact interaction. In this case one finds, as discussed in Appendix C, that the pairing matrix elements are separable, and the ground state energy can be determined by solving a simple dispersion relation, Eq. (C.6). We have tested our computer program in this way for different choices of the stength of the pairing interaction and for different cutoffs in the two-particle spectrum.

The last test is to see whether the free interaction (2.6) of -831 MeV fm^3 does indeed produce a bound state at zero energy. This can be checked by setting the strength of the single-particle potential, as well as the density dependent part of the pairing interaction, to zero. The results are shown in Fig. 2a, where the smallest correlated two-particle energy is shown as a function of the energy of the lowest single-particle state. This is a $0s_{1/2}$ continuum state and its energy is varied by changing the size of the radial box, here from 20 to 40 fm. The straight line is shown to guide the eye, whereas the points are the calculated values. It is seen that the two-particle energy extrapolates to zero in the limit of an infinitely large radial box. This may not be a very convincing test. The results for a weaker interaction would also extrapolate to zero. We have therefore repeated the calculations and required that the bound state should appear at $E_b = -0.5$ MeV. This implies a slightly stronger effective interaction. Repeating the derivation given in Section 2 one finds,

$$v_0 = -2\pi^2 \left(\frac{\hbar^2}{m}\right)^{3/2} E_c^{-1/2} \left(1 - \sqrt{\frac{-E_b}{E_c}} \operatorname{Arc\,tan} \left(\sqrt{\frac{E_c}{-E_b}}\right)\right)^{-1}, \tag{3.9}$$

which is -993 MeV fm^3 in the present case. The results are shown in Fig. 2b, and they are seen to extrapolate to -0.5 MeV in the limit of an infinite box.

4. Pairing in *p*-shell Nuclei

We shall apply the Green's function method outlined in the previous section to calculate the effect of pairing between two loosely bound neutrons in light nuclei. The most interesting case at present is ^{11}Li, since it is very weakly bound; the two-neutron separation energy is $S_{2n} = 0.25 \pm 0.10$ MeV [4, 5] and ^{10}Li is unbound by 0.8 ± 0.25 MeV [6]. We discuss this nucleus in more detail (ground state density and the dipole response) in the following sections. Here we shall first study

the pairing in two neighboring nuclei, ^{12}Be and ^{14}C, in order to adjust the parameters v_ρ and P of the pairing interaction (2.1). Having fixed the parameters we can then make predictions for other p-shell nuclei. We shall mainly consider nuclei that contain $N=8$ neutrons.

The appoach is to calculate the effect of pairing between two valence neutrons explicitly, whereas the residual interactions with the core (as well as among the core nucleons) are ignored. It is difficult, however, to choose a common single-particle Hamiltonian that gives a reasonable estimate of the core states and at the same time gives an accurate description of the two valence neutrons for which the pairing is turned off. We shall therefore use two different single-particle potentials, one for the core and one for the valence neutrons.

4.1. *Single Particle Potentials*

The single-particle potential, including spin-orbit, is parameterized in the usual way [7],

$$U(r)=V\left(1-0.44r_0^2(l\cdot\mathbf{s})\frac{1}{r}\frac{d}{dr}\right)\left[1+\exp\left(\frac{r-R}{a}\right)\right]^{-1}, \tag{4.1}$$

with $a=0.67$ fm, $R=r_0(A-2)^{1/3}$, and $r_0=1.27$ fm. Note that the radius is calculated as a function of the core mass, $A-2$. For a proton this is supplemented with the Coulomb interaction with the other $(Z-1)$ protons, represented by a uniformly charged sphere.

The strength of the potential for core nucleons is adjusted to give a reasonable estimate of the binding of the $0p_{3/2}$ proton and neutron states in p-shell nuclei which contain $N=8$ neutrons. We have chosen

$$V=-52+33\frac{N-Z}{A}\tau_3, \tag{4.2}$$

which is close to the value commonly used [7]. The calculated binding energies for the $0p_{3/2}$ neutron states compare well to the neutron separation energies of the associated $N=6$ p-shell nuclei (from Ref. [8]) or, when available, to a more realistic estimate based on the lowest $3/2^-$ neutron hole states in the corresponding $N=7$ isotopes (see Ref. [9]). The calculated binding energies of $0p_{3/2}$ proton states give the smooth trend of the measured proton separation energies for p-shell neuclei with $N=8$ neutrons. The data are strongly affected by proton pairing but we shall not try to improve on this aspect of the proton binding. All we need for our pairing calculation is a reasonable estimate of the nuclear core density which is an input to the interaction (2.1).

The single-particle potential for the valence neutrons is parametrized in the same way as in Eq. (4.1). The strength of the potential, however, is adjusted in each case so that the binding energy of the $0p_{1/2}$ state in a nucleus with $N=8$ neutrons reproduce the neutron separation energy of the associated $N=7$ isotope. This

choice is a natural starting point for calculating the effect of pairing between the two valence neutrons. The nucleus ^{11}Li causes a minor problem since ^{10}Li is unbound by 0.8 MeV. The strength of the single-particle potential is therefore adjusted so that the resonant $p_{1/2}$ state appears at that energy, which is achieved for the strength $V = -30.2$ MeV.

4.2. *Correlated Two-Neutron Binding Energies*

Given the core density and a single-particle potential for the valence neutrons we can now perform the pairing calculations described in Section 3. The ground state energy of the correlated pair, ε_{2n}, is determined as the lowest energy for which Eq. (3.7) has a maximum. The uncorrelated two-particle states, which appear in the matrix element of Eq. (3.7), are chosen to be the product of the two $0p_{1/2}$ states, coupled to $J=0$ as described in Appendix A.

We still need to specify the density-dependent parameters P and v_ρ in the pairing interaction, Eq. (2.1). Without the density dependence, the free interaction would produce extremely large pairing effects. For example, the expectation of our free interaction in the $(pp)^{L=0,S=0}$ shell model state of a harmonic oscillator is

$$\langle pp|\, v_0\, \delta(\mathbf{r}_1 - \mathbf{r}_2)\, |\, pp\rangle_{L=S=0} = \frac{5}{4} v_0 \left(\frac{m\omega_0}{2\pi\hbar}\right)^{3/2}. \tag{4.3}$$

The value of this matrix element is -15.8 MeV for $\hbar\omega_0 = 16$ MeV, which is much larger than the value of -6.9 MeV deduced from a systematic study of p-shell binding energies [10]. As mentioned earlier, will shall fit the density dependent parameters to the nuclei ^{14}C and ^{12}Be, which like ^{11}Li have eight valence neutrons. The best fit is obtained for $P = 1.2$ and $v_\rho = 930$ MeV fm^3. These are the parameters we shall use in the following, unless otherwise stated. We note that this interaction is slightly repulsive at nuclear matter density.

TABLE I

Calculated Two-Neutron Binding Energies ε_{2n} Compared to the Measured Separation Energies S_{2n}

Nucleus	$\varepsilon_{p_{1/2}}$ MeV	ε_{2n} MeV	S_{2n} MeV	Δ_{calc} MeV	Δ_{exp} MeV
^{10}He	+1.14	0			
^{11}Li	+0.80	−0.20	0.25 ± 0.10	1.80	1.85
^{12}Be	−0.504	−3.68	3.673	2.67	2.665
^{13}B	−3.370	−10.08	8.248	3.34	1.508
^{13}B*	−2.774	−8.72	8.248	3.17	2.700
^{14}C	−4.946	−13.10	13.123	3.21	3.231
^{16}O	−13.222	−29.57	28.886	3.12	2.442

Note. The adopted single-particle energies of the valence neutrons, $\varepsilon_{p_{1/2}}$, are also shown. The calculated and measured additional binding energies due to pairing, Eq. (4.4), are compared in the last two columns.

Having determined the interaction we can now make predictions for other p-shell nuclei. Some results are shown in Table I. The first column is the (uncorrelated) single-particle energy $\varepsilon_{p_{1/2}}$ of the valence neutrons, which has been adjusted to reproduce the neutron separation energy of the associated $N=7$ isotope [8]. Also shown is the calculated two-neutron binding energy, ε_{2n}, which is compared to the measured two-neutron separation energy S_{2n} [8]. A more interesting quantity is the additional two-neutron binding,

$$\Delta = 2\varepsilon_{0p_{1/2}} - \varepsilon_{2n}, \tag{4.4}$$

which is generated by the correlations. In the last two columns of Table I we compare the calculated additional binding energies to the corresponding values extracted form measured one- and two-neutron separation energies. It is seen that the predicted binding of ^{11}Li is in good agreement with the experimental value. Moreover, ^{10}He turns out to be unbound which is consistent with the present experimental knowledge [11]. The calculation for the tightly bound nucleus ^{16}O is surprisingly good considering the fact that other correlations may be important in this nucleus. The nucleus ^{13}B, on the other hand, deviates from the systematic trend; the additional binding obtained from our calculation is about two times larger than the value extracted from the measured separation energies. The reason is that the single-particle energy in this case is the separation energy of an odd–odd nucleus, ^{12}B. The ground state of this nucleus includes the correlation energy between the valence neutron and proton. If we remove this correlation by taking the statistically weighted separation energies of both $(p_{1/2}\, p_{3/2})^J$ states ($J=1, 2$) and use it to estimate the $0p_{1/2}$ single-particle energy, the disagreement is reduced to 0.5 MeV. This estimate is shown as ^{13}B* in Table I.

The sensitivity of the results to the parameters of the pairing interaction is illustrated in Table II. The strength of the density dependent term, v_ρ, has been adjusted for different choices of the parameter P so that the measured two-neutron separation energy of ^{14}C is reproduced. The binding of ^{12}Be is not so senstitive towards the shown variation of the parameters. The binding of ^{11}Li, on the other

TABLE II

Sensitivity of the Calculated Two-Neutron Binding Energy to Parameters of the Pairing Interaction, Eq. (2.1), for ^{12}Be and ^{11}Li

P	v_ρ(MeV fm^3)	ε_{2n}(^{12}Be) MeV	ε_{2n}(^{11}Li) MeV
0.5	600	−3.23	0
1.0	830	−3.59	−0.125
1.2	930	−3.68	−0.20
1.5	1080	−3.80	−0.29
Experiments		−3.67	−0.25 ± 0.10

hand, is quite sensitive, ranging from unbound to values within the uncertainty of the measured two-neutron separation energy.

The calculations discussed above were performed on a finite radial grid (see Section 3). The radial wave functions were required to vanish at the maximum distance, so the continuum states are actually discrete. All possible single-particle states, except those that are occupied by the core neutrons, were included in the construction of the two-particle Green's function (3.8). The possible states are constrained by the condition that the two-particle energy is less than $E_c = 40$ MeV, which is the energy cutoff that was used to determine the free interaction in Section 2. The bound states of the core, on the other hand, were matched to the analytic asymptotic expressions that are valid outside the nuclear interaction region. The core density is therefore not affected by the radial cutoff. We have checked that the results for ^{12}Be and ^{14}C are insenstitive to the radial cutoff (in the range from 15 to 30 fm), and to the step size (from 0.1 to 0.5 fm).

4.3. *Results for* ^{11}*Li*

It is remarkable that we are able to predict the two-neutron separation energy of ^{11}Li so accurately by adjusting the pairing interaction to reproduce the effect of pairing in ^{12}Be and ^{14}C considering the uncertainties involved and the approximations we have made. In this connection it is interesting to study the senstitivity of this result towards the choice of the $p_{1/2}$ resonance energy. This is illustrated in Fig. 3, where the correlated two-neutron energy is shown as a function of the $p_{1/2}$ single-particle energy, ranging from bound states to resonant states. This variation was achieved by changing the depth of the valence, single-particle potential. It is also interesting to see the sensitivity to the core recoil. The simplest calculation we can make in our approach is to use the effective mass $m(A-2)/(A-1)$ in the single-particle Hamiltonians. This accounts for the core recoil for two uncorrelated valence neutrons. The dashed curve in Fig. 3 is the result we obtain when we make this change. The calculation requires a new calibration of the density dependent part of the interaction (2.1) in order to reproduce the two-neutron binding in ^{12}Be and ^{14}C. The best fit is obtained with the parameters $P = 3.1$ and $v_\rho = 1710$ MeV fm^3. The predicted two-neutron binding in ^{11}Li is now reduced to 100 keV.

The highest point in Fig. 3 (open circle) has a positive value, $\varepsilon_{2n} = +0.14$ MeV. This is the result obtained with a radial cutoff at 40 fm. The value of ε_{2n}, however, decreases slowly with an increasing radial cutoff distance. It should finally converge to a value less than (or equal to) zero, since the free interaction has been chosen to produce a bound state at zero energy. The negative two-neutron energies shown in Fig. 3 are more reliable. Although the calculated values fluctuate with different choices of the radial cutoff, the average value is fairly constant. Moreover, the fluctuations are reduced as the box size is increased, and they are of the order of 0.01 MeV at a 40 fm box size.

From Fig. 3 we see that the range of the neutron resonance energy in ^{10}Li, of 0.8 ± 0.25 MeV (cf. Ref. [6]), is equivalent to a two-neutron separation energy in

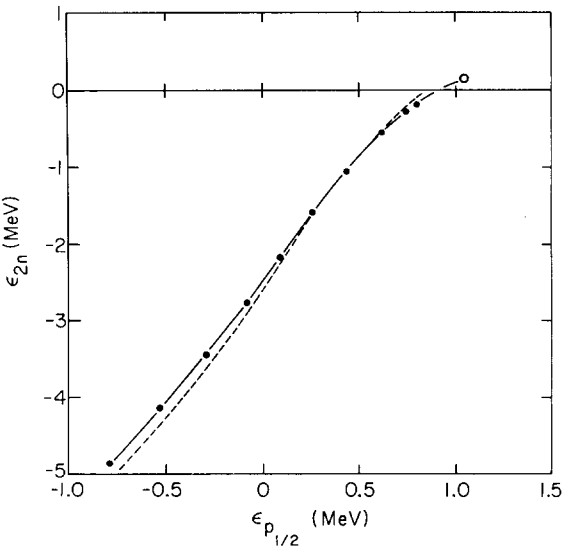

FIG. 3. Correlated two-neutron energy of the ground state of ^{11}Li as a function of the $p_{1/2}$ single-particle energy. The latter energy was varied (from bound states to resonant states) by changing the depth of the valence potential. The results shown have been calculated with a radial cutoff of up to 40 fm. The result with a positive two-neutron energy has not converged as explained in the text. The dashed curve was obtained as described in the text using an effective nucleon mass of $m(A-2)/(A-1)$, which accounts for the core recoil associated with two uncorrelated valence neutrons.

the range from zero to 0.7 MeV. Choosing the resonant energy exactly at 0.8 MeV produces a two-neutron separation energy of 0.20 MeV, which is consistent with the measured value of 0.25 ± 0.10 MeV, cf. Ref. [4, 5]. The ground state of the pair is constructed entirely from continuum states with a dominant constribution from p-states. It is composed of 6.1% s-states, 3.9% $p_{3/2}$, 76.9% $p_{1/2}$, 7.4% $d_{5/2}$, and 2.5% $d_{3/2}$ states, while the rest is in higher angular momentum states. Note that the $s_{1/2}$ and the $p_{3/2}$ components are orthogonal to the occupied $s_{1/2}$ and $p_{3/2}$ core states.

4.4. *Results for* ^{14}*Be*

Another example on a loosely bound, neutron rich nucleus is ^{14}Be. The measured two-neutron separation energy is 1.3 MeV [5], whereas ^{13}Be is unbound. We have performed similar pairing calculations for the two valence neutrons in this nucleus, assuming that the core, ^{12}Be, can be described by the single-particle potential (4.1)–(4.2). To our knowledge there is no information about resonant states in ^{13}Be so we are not able to calibrate the valence single-particle potential as we did for the other p-shell nuclei discussed earlier. We shall therefore present our results as a function of the calculated $0d_{5/2}$ resonance energy. The results are shown in Fig. 4. The measured two-neutron separation energy is reproduced for a resonant energy

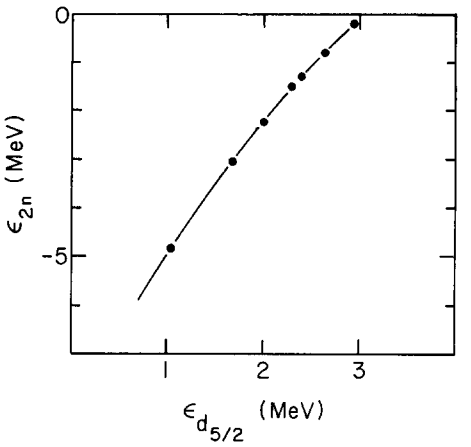

FIG. 4. Correlated two-neutrons energy of the ground state of ^{14}Be as a function of the $d_{5/2}$ resonance energy, which was varied by changing the depth of the valence neutron potential.

of $\varepsilon_{d_{5/2}} = 2.4$ MeV. The nucleus remains bound up to a resonant energy of 3 MeV, and the two-neutron separation energy is 5 MeV when the $1s_{1/2}$ state starts to become bound. The ground state of the pair that reproduces the measured two-neutron separation energy has a much larger fraction of s- and d-states than ^{11}Li has. It contains 18.9% s-states, 2.5% $p_{3/2}$, 1.1% $p_{1/2}$, 62.4% $d_{5/2}$, and 7.6% $d_{3/2}$ states, and the occupied core states are here explicitly excluded.

4.5. *Other* 0^+ *states*

The Green's function method also allows us to study excited states. Of particular interest is ^{14}C for which two excited 0^+ states have been measured, at an excitation energy of 6.59 and 9.75 MeV [9], respectively. In this nucleus, the continuum starts at 8.1 MeV excitation. Our calculated 0^+ spectrum contains a correlated state at an excitation energy of about 9.6 MeV, together with other states which are essentially continuum states in our discretized representation. These states mix when they are within a few hundred kiloelectron volts of each other. The average position of the correlated state, however, is fairly insensitive to the location of the other states. Since we find no correlated excited state lower than 9.6 MeV, our model cannot explain both measured states.

It is interesting to see whether these nuclei are likely to exhibit the Efimov effect [12]. This is the prediction that a three-body system will have a large number of levels provided the two-body forces are of resonant nature. These states would be extended and very weakly bound, just below the three-body breakup threshold. This phenomenon might occur in neutron-rich nuclei when the approximations we have made are applicable. The force between the two valence neutrons almost make them a bound system, and if the binding energy of the lowest valence states were

close to zero the conditions for the effect would be fulfilled. This is unfortunately not the case for any of the p-shell nuclei shown in Table I.

A more promising case is the nucleus ^{14}Be. We find that if the lowest valence neutron state (the $1s_{1/2}$ state) is put close to zero, the $d_{5/2}$ resonance energy is about 1 MeV and the ground state of the two-neutron system is bound by 5 MeV, cf. Fig. 4. For the Efimov effect to be present, there would have to be additional bound states with very small binding. We do find a single additional 0^+ state with a two-neutron binding energy of only 180 keV. This state disappears into the continuum if the single-particle energy is increased a small amount. Thus, with an impirical two-neutron separation energy in the ground state of only 1.3 MeV, it is very unlikely that the nucleus ^{14}Be exhibits the Efimov effect.

5. Correlated Ground State Density for ^{11}Li

In this section we shall discuss and illustrate the correlated ground state density of the two valence neutrons in ^{11}Li. The fact that the two-neutron separation energy is so small for this nucleus makes it difficult to estimate the valence density in a simple shell model approach. In particular, it is uncertain what one should choose for the single-particle binding energy. Previous estimates have been based on a $0p_{1/2}$ binding energy ranging from 0.2 to 1.0 MeV (see Refs. [13–15]). We can address this question more realistically from our pairing calculations.

In the previous section it was demonstrated that a pairing calculation, based on the effective interaction (2.1), can account quite accurately for the two-neutron binding in ^{11}Li, when the parameters of the interaction are adjusted to fit the pairing of the two valence neutrons in ^{12}Be and ^{14}C. We shall use these optimum parameters ($P = 1.2$ and $v_\rho = 930$ MeV fm^3) in the following to determine the density. The core density, which enters into the expression for the effective interaction, is calculated as described in Section 4.1. The calculations have been performed on a radial grid, from zero to 40 fm in steps of 0.25 fm. The correlated ground state energy of the neutron pair converged in this case to a value of -0.20 MeV. It is very important to use such a large radial cutoff in order to obtain an accurate estimate of the tail of the density.

The correlated two-particle wave function is given by

$$\Psi_{gs}(\mathbf{r}_1, \mathbf{r}_2) = \sum_{nn'lj} \alpha_{nn'lj} \Psi^{(2)}_{nn'j}(\mathbf{r}_1, \mathbf{r}_2). \tag{5.1}$$

This is an expansion on two-particle shell model wave functions which are coupled to a total spin of $J = 0$. The construction of these states is discussed in Appendix A, and Eq. (A.4) gives the general expression. The amplitudes $\alpha_{nn'lj}$ can be obtained either from a diagonalization of the two-particle Hamiltonian (3.1), or from the two-particle Green's function method discussed in Section 3. In the latter case one can extract the amplitudes from Eq. (3.7), which was used to determine the ground

state energy in Section 4. We have in fact used both methods and found that they give essentially identical results when the parameter η in Eqs. (3.7)–(3.8) is chosen sufficiently small. We prefer the Green's function method since it appears to be the faster for a large radial box.

Once the amplitudes have been determined, the one- and two-particle densities for the ground state of the pair can be calculated as described in Appendix B. The most detailed information is contained in the two-particle density $\rho_2(r_1, r_2, \theta_{21})$, which is a function of the radial coordinates of the two particles with respect to the center of the core, and the angle θ_{21} between their positions. This density, weighted

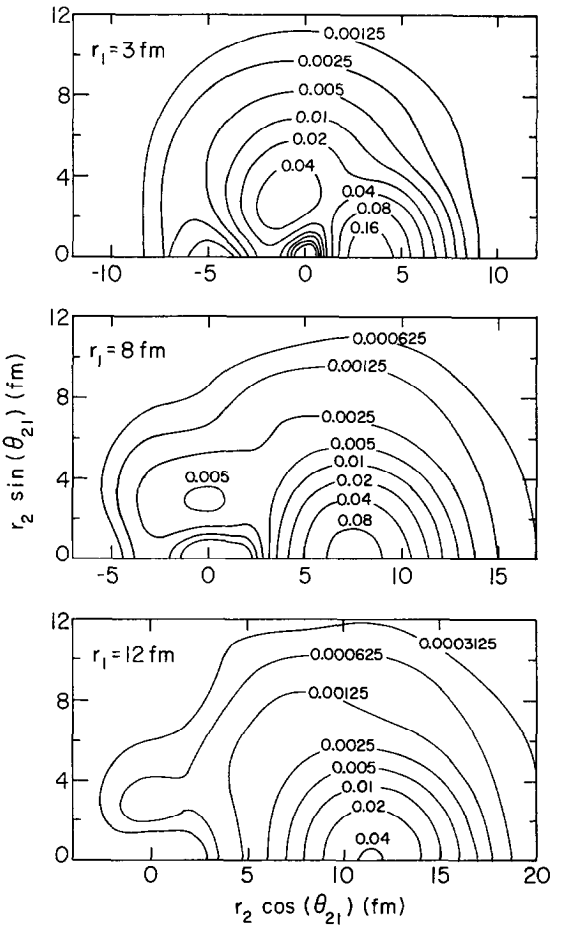

FIG. 5. Contour plots of the two-particle density of the valence neutrons in ^{11}Li. The density has been weighted by $4\pi r_1^2 4\pi r_2^2$, and it is illustrated (in units of fm^{-2}) for three different positions r_1 of one the neutrons. The contours are shown as functions of the coordinates $(r_2 \cos(\theta_{21}), r_2 \sin(\theta_{21}))$ of the second neutron.

by the factor $4\pi r_1^2 4\pi r_2^2$, is illustrated in Fig. 5 by countour plots for selected values of the radial distance r_1 of one of the particles.

The density appears to be fairly complicated when one of the particles is required to be close to the core. Then there are two peaks, one close to the selected particle, and one at $\theta_{21} = 90°$. The latter peak is associated with the $S = 1$ component of the two-particle wave function, whereas the peak near the selected particle is dominated by the $S = 0$ component. These features can be explained in the following way. The two-particle density is a simple sum of the two spin components, as can be seen from Eq. (B.8). Equation (B.6) shows that the angular dependence of the $S = 1$ component is constructed from the spherical harmonics $Y_{l,1}(\theta_{21})$, which all vanishes at $\theta_{21} = 0$. The peak near the selected particle is therefore mainly $S = 0$. On the other hand, our calculations show that the p-states constitute about 84% of the ground state. The $S = 0$ component of this part of the ground state wave function is proportional to $\cos(\theta_{21})$, which vanishes at $\theta_{21} = 90°$.

When one of the particles is required to be far away from the core the correlation between the two particles appears to be a much more dominant feature, as can be seen in Fig. 5 for $r_1 = 12$ fm. The peak at $\theta_{21} = 90°$ has almost disappeared and it is a factor of 60 smaller than the main peak. Our calculations show that the $S = 0$ and $S = 1$ components of the correlated ground state are almost equal. The $S = 1$ component, however, falls off much faster than the $S = 0$ component. It constitutes 59% of the single-particle density at $r_1 = 3$ fm and has descreased to 21% at 12 fm.

It is interesting to compare the shape of the main peak to the shape obtained from the zero energy state of two neutrons discussed in Section 2. The wave function

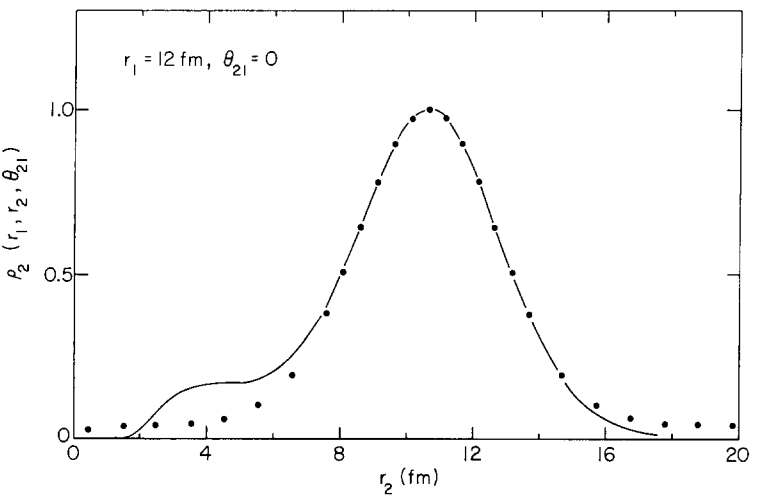

FIG. 6. Two-particle density of the valence neutrons in ^{11}Li as a function of the position r_2 of one of the neutrons, for a fixed $r_1 = 12$ fm and $\theta_{21} = 0$. The density has been normalized to one at the maximum. It is compared to the correlated density for free neutrons (dots, obtained from Eq. (2.7)), which has been shifted to match the position of the maximum.

for this state is given by Eq. (2.7), and the associated density is shown as dots in Fig. 6. It has been shifted to fit the position of the maximum which appears at 10.65 fm. It is compared to the calculated two-particle density $\rho_2(r_1 = 12, r_2, \theta_{21} = 0)$ (fully drawn curve), which has been normalized to one at the maximum. The agreement near the peak position is remarkably good. The width of the peak is completely determined by the cutoff in the two-particle energy spectrum that we have been using. This can be seen from the analytic expression Eq. (2.7). The calculated density is seen to have a shoulder in the range of 3 to 6 fm, and falls off rapidly at smaller distances near the radius of the core, which is 2.64 fm.

The single-particle density, weighted by $4\pi r^2$, is illustrated in Fig. 7. The fully drawn curve is the result for a radial cutoff at 40 fm, whereas the two dashed curves show the results obtained for a cutoff at 20 and 30 fm, respectively. The comparison clearly shows the importance of having a large radial cutoff in order to obtain a reliable tail of the single-particle density. The density near the maximum, on the other hand, is rather insensitive to the radial cutoff. We have mentioned earlier the question of which single-particle energy one should use for the two valence neutrons in ^{11}Li in a simple shell model calculation. In order to answer this question we have tried to fit the density with that of a $p_{1/2}$ state bound in a Woods–Saxon potential of the form (4.1). The best overall fit, which is indicated by dots in the figure, was obtained by increasing r_0 to 1.52, and using a depth of $V = -26.53$ MeV. This yields a single-particle energy of -0.296 MeV, not far from

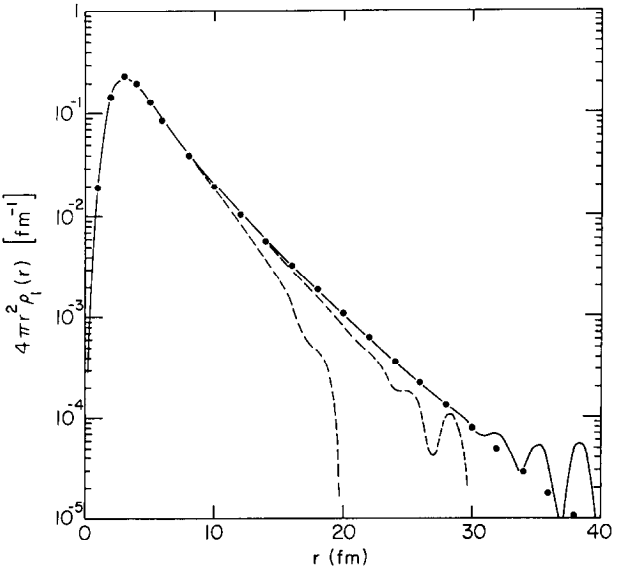

FIG. 7. Single-particle density of the valence neutrons in ^{11}Li, weighted by $4\pi r^2$. The radial cutoff is 20 and 30 fm for the two dashed curves, and it is 40 fm for the fully drawn curve. The dots represent the best $p_{1/2}$ shell model fit, obtained as described in the text.

the two-particle binding energy. The fit deviates from the calculated density by less than 10% in the range from 0 to 30 fm. Thus a single-particle binding energy of 1 MeV, which is the apparent binding energy with respect to ^{10}Li, is quite unrealistic.

In the dineutron model, the wave function is assumed to have a fixed internal structure of the neutron pair, and the pair's center of mass motion is characterized by a binding energy and an exponential decay at large distances. We can study the effective binding of the pair by plotting the two-particle density as a function of the center of mass coordinate of the two neutrons at zero relative separation, i.e., $r_1 = r_2$. This density, weighted by the factor $4\pi r_1^2 4\pi r_2^2$, is illustrated in Fig. 8. It decays exponentially in the range from 4 to 20 fm with a decay constant of 0.23 fm^{-1}, which is equivalent to a two-particle energy of $\varepsilon_{2n} = -0.14$ MeV. This value differs slightly from the ground state energy of the pair of -0.20 MeV, determined in Section 4. However, one should not expect to have a simple, exact relationship between the radial decay and the binding energy since the structure of the two-particle density shown in Fig. 5 is fairly complicated. This remark applies as well to the single-particle density discussed above.

It is interesting to compare our results to those of Johannsen *et al.* [16] obtained from a three-body variational calculation. The interaction between the valence neutrons was adjusted to reproduce low energy scattering data, i.e., the scattering length and the effective range. Their neutron–core interaction is not as realistic as

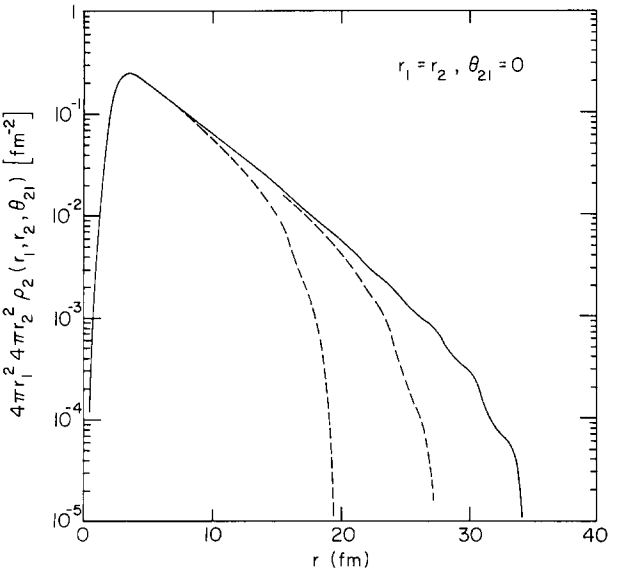

FIG. 8. The two-particle density of the valence neutrons in ^{11}Li, weighted by $4\pi r_1^2 4\pi r_2^2$, is shown at identical particle positions, $r = r_1 = r_2$ and $\theta_{21} = 0$. It is shown for three different radial cutoffs of 20, 30, and 40 fm, respectively.

TABLE III

Moments of the Two-Neutron Density Obtained in the Single-Particle Model and in the Three-Body Model, Which Includes the Effect of Pairing, Given for Different Radial Cutoffs, r_{max}

Model	r_{max} (fm)	$\langle r^2 \rangle$ (fm^2)	$\langle \lvert \mathbf{r}_1 + \mathbf{r}_2 \rvert^2 \rangle$ (fm^2)	Total strength (e^2 fm^2)
Single-particle	12.5	18.5	37.0	0.66
Single-particle	40	34.1	68.2	1.21
Three-body	40	34.1	97.4	1.73

Note. The associated total dipole strengths, Eq. (7.3), are given in the last column.

ours. They concentrated on the relation between the mean square radius $\langle r^2 \rangle$ and the two-neutron binding energy and represented variations of the single-particle potential by the increment,

$$\delta \langle r^2 \rangle = \langle r^2 \rangle_{11} - \tfrac{9}{11} \langle r^2 \rangle_9, \tag{5.2}$$

of the mean square radius of ^{11}Li with respect to ^{9}Li. Their variables, ρ and λ, are equivalent to $\mathbf{r}_1 - \mathbf{r}_2$ and $\frac{1}{2}(\mathbf{r}_1 + \mathbf{r}_2)$ in our notation. The mean square values we obtain for these variables, $\langle \rho^2 \rangle = 39$ and $\langle \lambda^2 \rangle = 24.4$ fm^2, can be extracted from the last row of Table III. They imply an increament of $\delta \langle r^2 \rangle = 5.4$ fm^2. Combined with our calculated two-neutron binding energy of 0.20 MeV, this is in very good agreement with their results and the experimental information that they quote (see Fig. 3 of Ref. [16]). Their parameters imply a ^{10}Li neutron resonance energy of 300 keV. Our single-particle potential, on the other hand, was adjusted to reproduce the measured resonance energy of 800 keV.

6. Pairing in Infinite Nuclear Matter

It is also of interest to consider pairing in infinite nuclear matter and to compare to recent Hartree–Fock calculations based on the Gogny force [17]. The gap equation is much simpler in our model, where we use the zero-range, density dependent pairing interaction (2.1). Here we shall assume that the single-particle states are plane waves with energies $\varepsilon(k) = (\hbar k)^2/2m$. The constraint on the two-particle energy spectrum discussed in Section 2 implies a cutoff in the single-particle spectrum at $\varepsilon_c = \frac{1}{2} E_c$. Thus the gap equation is (cf. Eq. (8) of Ref. [17]),

$$\Delta = -\frac{1}{2} v_{\text{eff}}(\rho) \int_{\varepsilon(k) \le \varepsilon_c} \frac{d\mathbf{k}}{(2\pi)^3} \frac{\Delta}{\sqrt{(\varepsilon(k) - \varepsilon_F)^2 + \Delta^2}}, \tag{6.1}$$

where ε_F is the Fermi energy and Δ is the pairing gap.

We can express this equation in terms of an integral over the single-particle energies and eliminate some of the constants using the condition (2.6) for the free interaction. This leads to the following equation for the pairing gap,

$$1 = \frac{1}{2}\frac{v_{\text{eff}}(\rho)}{v_0}\frac{1}{\sqrt{\varepsilon_c}}\int_0^{\varepsilon_c} d\varepsilon \sqrt{\varepsilon/((\varepsilon-\varepsilon_F)^2+\Delta^2)}. \tag{6.2}$$

This equation is fairly simple to solve numerically. We note that the pairing gap vanishes in the limit $\rho = 0$. This is due to the fact that we have chosen the interaction (2.1) so that $v_{\text{eff}}(\rho = 0) = v_0$; i.e., the free interaction produces a bound state of the pair at zero energy.

The pairing gap is shown in Fig. 9a as a function of the Fermi momentum. The points are the results obtained from the Gogny force in Ref. [17]. The fully drawn curve is our result obtained with the parameters for the pairing interaction (2.1) determined in Section 4. We note that there are only three parameters that deter-

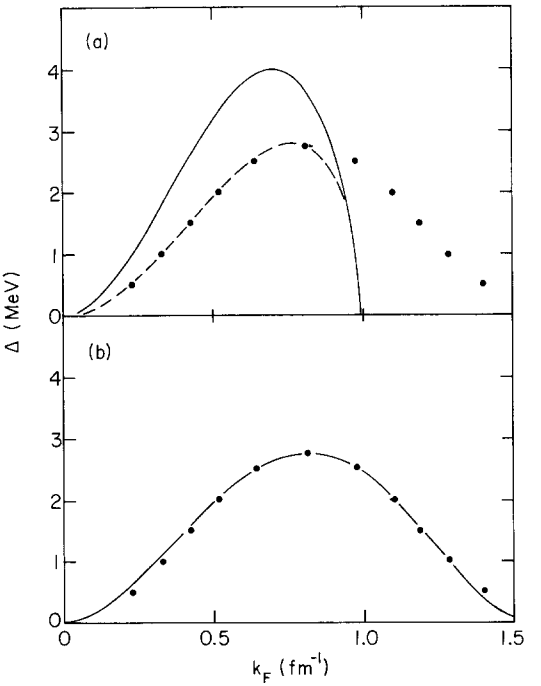

FIG. 9. Pairing gap in infinite nuclear matter as a function of the Fermi momentum. The dots are the results of a Hartree–Fock calculation using the Gogny force (from Ref. [17]). The fully drawn curve in (a) is the result obtained with our effective pairing interaction (2.1), using the parameters determined in Section 4. The dashed curve is a fit to the Gogny-force results at low densities, obtained by adjusting the interaction parameters as described in the text. An overall fit to the Gogny-force results, obtained by adjusting both the energy cutoff and the parameters of the interaction, is shown in (b).

mine the pairing gap at a given density. They are the energy cutoff ε_c (20 MeV), the power of the density dependence P (1.2), and the ratio between the density dependent coefficient and the free interaction ($v_\rho/v_0 = -930/831$). It is seen that our pairing gap vanishes for $k_F \geqslant 1$. This is due to the small value of the energy cutoff. This choice is limited by the number of two-particle states that we are able to handle in the calculations for finite nuclei.

We can adjust our interaction so that we reproduce the results from the Gogny force, at least in the low density region, with the same energy cutoff. This is illustrated by the dashed curve in Fig. 9a. The parameters needed to make this fit are $v_\rho/v_0 = -0.45$ and $P = 0.25$. This interaction is clearly weaker than our empirical interaction in most of the density range, where the gap is non-zero. The fact that we are able to fit the results from the Gogny force so that the pairing gap vanishes at zero density, and not at a small, non-zero density, implies that the Gogny force resembles a realistic free interaction in the low density limit.

It is also possible to reproduce the results from the Gogny force over a wider range of densities by increasing the energy cutoff. This is illustrated in Fig. 9b. The parameters of the interaction are here, $\varepsilon_c = 60$ MeV, $v_\rho/v_0 = -0.7$, and $P = 0.45$. It would be very difficult to perform the calculations presented in Sections 4 and 5 with such a high energy cutoff.

7. Dipole Response

Weakly bound neutrons can be easily excited by an external dipole field. The neutrons have an effective charge of $-eZ/A$ in the center of mass system, and their spatial extension gives them transition dipole moments which can be large compared to typical nuclear $E1$ transitions [18]. In fact, the experimentally deduced Coulomb excitation of ^{11}Li shows a dramatic order-of-magnitude enhancement compared to tightly bound nuclei [19]. To model these transitions, the numerical grids must extend to much larger distances than one is accustomed to using. We shall first illustrate this point with a simple independent-particle model for the ^{11}Li dipole response.

In the model, the ground state is described by a pair of neutrons in the $p_{1/2}$ orbit. The wave function ϕ_b is determined by a single-particle Hamiltonian with a Woods–Saxon potential. The radius of the potential is that typical for an $A = 9$ nucleus, and the depth is chosen to fix the separation energy E_b. The final state makes use of the same single-particle Hamiltonian, with one particle in a continuum orbit. The continuum wave function ϕ^c_{lj} has a positive energy E, and is normalized to the convention given in Appendix D. Then the $B(E1, \uparrow)$ is given by

$$\frac{dB(E1,\uparrow)}{dE} = 2\left(\frac{Z}{A}\right)^2 e^2 \sum_{j=1/2,\,3/2} \frac{2j+1}{4\pi}\left(\frac{1}{2}\,\frac{1}{2}\,j\,-\frac{1}{2}\,\middle|\,10\right)^2 \left|\int_0^\infty \phi_b \phi^c_{lj} r^3\, dr\right|^2. \qquad (7.1)$$

It should be emphasized that the choice of separation energy in the model is

ambiguous; physically the pairing rather than the single-particle potential provides the binding. However, the effects of the pairing may be to provide an effective single particle binding of the order of magnitude of the two-particle binding, $E_b \sim 0.2$ MeV. Using this value for the single-particle separation energy, we show in Fig. 10 the predicted dipole strength calculated from Eq. (7.1). Results are given for two values of the spatial cutoff: first with the single-particle wave function ϕ_b constructed on a grid extending to $r_{\max} = 12.5$ fm, with a boundary condition that $\phi_b(r_{\max}) = 0$, and then with the boundary extended to $r_{\max} = 40$ fm. The more accurate strength function has a sharp peak just above threshold due to the $p_{1/2} \to s_{1/2}$ transition to the continuum. The transition $p_{1/2} \to d_{3/2}$ is also significant above the threshold region. The strength then falls roughly as $1/E$ over a range of a few MeV. The sharp peak is completely absent from the calculation with the smaller cutoff radius. This illustrates the difficulty in constructing a realistic model of the response; a three-body wave function has to be constructed accurately in a domain extending to distances of the order of 40 fm.

Because the transition strength distribution is difficult to calculate with more realistic models, it is useful to define some integral properties of the response that can be computed without any knowledge about the final state wave functions. The first of these, the energy-weighted sum rule, is particularly convenient because it can be evaluated without knowing the wavefunction at all. In our basic model of the nucleus as a three-body system composed of two neutrons and an inert core, the energy-weighted sum rule reads

$$\int \frac{dB(E1,\uparrow)}{dE} E\, dE = 2\frac{9e^2}{4\pi}\left(\frac{Z}{A}\right)^2 \frac{\hbar^2}{2m}. \tag{7.2}$$

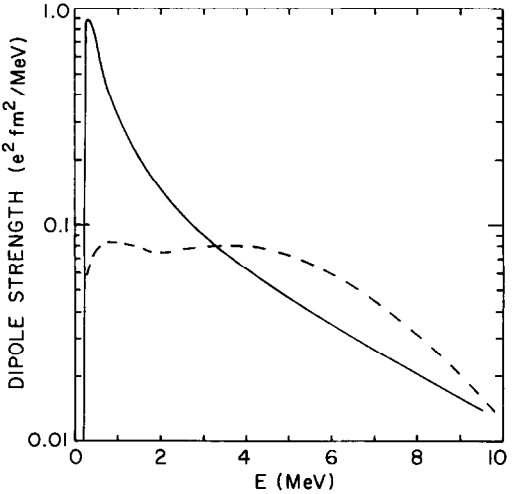

FIG. 10. Dipole strength of the valence neutrons in ^{11}Li as a function of the excitation energy. Both curves are independent particle responses, obtained as described in the text for a radial cutoff at 12.5 fm (dashed curve) and at 40 fm (fully drawn curve).

For ^{11}Li, the sum rule has the value 2.21 e^2 MeV fm^2. However, included in this sum will be unphysical transitions to occupied levels of the neutron–core Hamiltonian. To limit the sum rule to positive excitation energies, the negative contribution from the (Pauli forbidden) transitions to occupied states needs to be subtracted. In the above model the transition strength to the occupied $s_{1/2}$ orbit is 0.68 MeV fm^2, so the continuum sum rule becomes $2.21 + 0.68 = 2.89\, e^2$ MeV fm^2.

The integrated response without the energy weighting is also very useful and is more closely related to the measured cross sections. It can be calculated from the two-particle density of the ground state,

$$\int \frac{dB(E1,\uparrow)}{dE}\, dE = \frac{3e^2}{4\pi}\left(\frac{Z}{A}\right)^2 \int d\mathbf{r}_1\, d\mathbf{r}_2 \rho_2(\mathbf{r}_1, \mathbf{r}_2)(r_1^2 + r_2^2 + 2\mathbf{r}_1 \cdot \mathbf{r}_2). \tag{7.3}$$

For the independent particle model, the last term in the integrand does not contribute and the sum can be expressed as an integral over the single-particle density,

$$\int \frac{dB(E1,\uparrow)}{dE}\, dE = \frac{6e^2}{4\pi}\left(\frac{Z}{A}\right)^2 \langle r^2 \rangle. \tag{7.4}$$

The independent particle values of $\langle r^2 \rangle$ are shown in Table III, for the two boundary sizes. We see that making the boundary larger nearly doubles this expectation value. As discussed for the energy-weighted sum rule, the integrated response includes an unphysical contribution from the occupied $s_{1/2}$ state. This correction is only a few percent. We quote in Table III the integrated response obtained from Eqs. (7.3) or (7.4), which is a slightly higher upper limit.

An estimate of an average excitation energy associated with the dipole transition can be obtained by dividing the EWSR by the integrated response. This yields 2.4 MeV for $r_{\max} = 40$ fm, which is rather higher than one might guess looking at Fig. 10. Thus the sum rules have little value for estimating the peak of the response, because it has an extended tail going to high energy.

We now examine the strength function for the more realistic three-body model, in which the binding energy is due to the pairing interaction. There is practically no change in the continuum EWSR, because the bound–bound contribution depends mainly on the probabilities for the particle to be in the various single-particle orbitals. The $p_{1/2}$ probability is 77%, so the independent particle model, which assumes 100%, should be good enough to estimate this correction.

The integrated stength need not be close to the value calculated in the independent-particle model. First of all, the radial wave functions are not characterizable by a definite single-particle binding energy, and the expectation of r^2 in the single-particle density must be calculated anew. The three-body model gives a neutron density with the expectation value $\langle r^2 \rangle$ shown in Table III. It coincides accidentally with the value obtained in the independent-particle model. Although the asymptotic falloff of the single-particle density (discussed in Section 5) was found to be faster in the three-body model than in the single particle model

(with $E_b = E_s$), this is compensated by an effectively larger nuclear radius; the best fit to the single-particle density was obtained with a $p_{1/2}$ state bound by 0.3 MeV and a 20% larger nuclear radius.

The last term in Eq. (7.3), which vanished in the independent-particle model, will contribute to the integrated strength in the three-body model. In the limit of very strong correlations, this term would be equal in magnetiude to the first two terms and would double the integrated strength. However, the correlation is actually not so strong. The values quoted in Table III gives an increase of 43%. The total integrated strength obtained from Eq. (7.3) is shown in the last column of Table III.

To get more detailed information about the distribution of the dipole stength, we should calculate the matrix elements of the dipole operator between the ground and continuum excited states. Unfortunately, treatment of correlations in the continuum states is more difficult. The Green's function method for two-particle states in the continuum requires the solution of an integral equation with a principal value integral. The Hamiltonian matrix method requires a discrete basis, and the connection to a continuum strength distribution can only be made when there are many eigenstates in an interval of interest.

However, we are able to calculate the transition strength distribution neglecting the residual interaction in the final state. The formula for the differential transition strength in this approximation is given in Appendix D. We have evaluated it for the case with a boundary $r_{max} = 40$ fm. The double differential cross section in the range of 0–4 MeV is shown in Fig. 11. We see a ridge with neutron energy in the range 0.6–0.7 MeV. This corresponds to the physical process in which one nucleon is

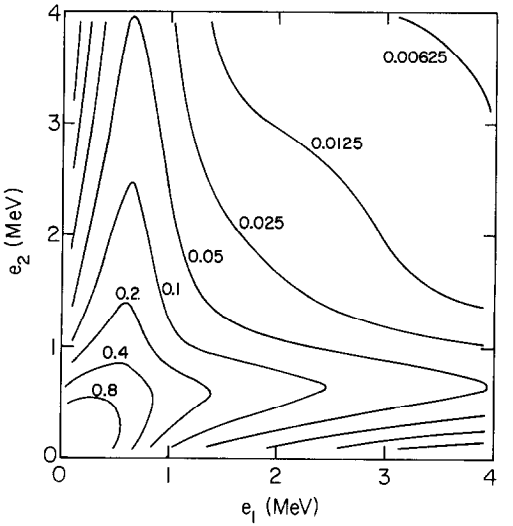

FIG. 11. Contour plot of the dipole strength of the correlated valence neutrons in ^{11}Li, Eq. (D.9), as a function of the energies of the two neutrons in the uncorrelated final state. The contour values are in units of e^2 fm^2/MeV^2.

excited and the other remains as a spectator in the $p_{1/2}$ single-particle resonance of ^{10}Li. Since 77% of the ground state probability is $p_{1/2}$, it is not surprising that there remains a strong signal of the single-particle shell physics in the predicted final state neutron spectrum. We next show the predicted differential transition strength with respect to excitation energy,

$$\frac{dB(E1,\uparrow)}{dE} = \int de_1\, de_2 \frac{dB(E1,\uparrow)}{de_1\, de_2} \delta(E - e_1 - e_2 + \varepsilon_{2n}), \tag{7.5}$$

where ε_{2n} is the calculated -0.20 MeV ground state energy of the pair. This strength is displayed in Fig. 12. We see that there is a fairly broad peak at about 1 MeV excitation, corresponding to the excitation energy of the ^{10}Li resonance. This contrasts sharply with the independent particle model, where the peak was just above threshold. Unfortunately, the calculation is unreliable on this important aspect of the strength distribution. The EWSR for the strength shown in Fig. 12 exceeds the continuum sum rule by 50%, which indicates that at least some of the strength in the 1 MeV peak should be shifted closer to threshold. The residual interaction in the final state probably plays a significant role. In the initial state, the interaction energy and the kinetic energy of the two neutrons nearly cancel, but only the positive kinetic energy is represented in the final state in our approximation. Clearly, it is desirable to further develop the numerical aspects of this study so that a more realistic description of the final state can be made.

One can get some guidance concerning the effect of correlations on the dipole response from the harmonic oscillator model discussed in Appendix C. One can show that the correlated final state, generated by dipole excitation, is determined by exactly the same dispersion relation as the correlated ground state. Moreover, the

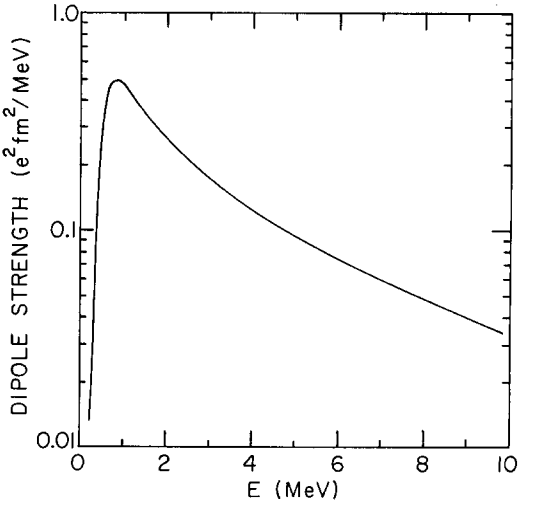

FIG. 12. Dipole strength of the valence neutrons in ^{11}Li as a function of the excitation energy. It was obtained by integrating the dipole strength distribution shown in Fig. 11 according to Eq. (7.5).

correlated dipole response is identical to the uncorrelated response, which is a simple $1\,\hbar\omega_0$ excitation. The dipole response from the correlated ground state to uncorrelated final states, on the other hand, has amplitudes to higher excitations. Thus the EWSR is larger due to the ground state correlations, whereas the total strength is the unchanged.

Let us finally discuss how the calculated dipole strength relates to recently measured fragmentation cross sections for ^{11}Li at 800 MeV per nucleon on heavy targets [19]. The measured cross sections are unusually large and can only be explained by postulating large electromagnetic dissociation cross sections σ_{EMD}. In particular, the measured (^{11}Li, ^{9}Li) breakup cross section on a Pb target is 1310 mb, and subtracting the estimated nuclear part of this cross section a value of $\sigma_{\mathrm{EMD}} = 890$ mb was deduced [19]. A major part of this cross section must originate from low-lying dipole strength. Relativistic Coulomb excitation favors dipole excitations and in particular to low excitations. The excitation of the giant dipole resonance, on the other hand, yields a cross section that is an order of magnitude smaller than the experimentally deduced value.

In a recent publication [15] we investigated the nuclear part of the fragmentation using an eikonal approximation and an independent particle model to describe the density of ^{11}Li. The independent particle model was very similar to the one we used to deduce the dipole response shown in Fig. 10 and assumed a $p_{1/2}$ binding energy of 0.2 MeV. We found that it was necessary to integrate to very large impact parameters in order to achieve convergence, much further than the smaller boundary mentioned in Table III. The calculated nuclear part of the (^{11}Li, ^{9}Li) breakup cross section was 710 mb for reactions on a Pb target. This implies the value $\sigma_{\mathrm{EMD}} = 600$ mb, which is significantly smaller than the originally deduced value. The sensitivity towards the assumed $p_{1/2}$ binding is illustrated in Fig. 4 of Ref. [15]. Although the independent particle model differs in several respects from the three-body model (as discussed above and in Section 5) it may not be too unrealistic when it comes to estimating of the nuclear part of the fragmentation. In fact, the two models give almost identical results for $\langle r^2 \rangle$, cf. Table III.

It is now interesting to compare this estimate to the predictions we can make based on the dipole strength distributions shown in Figs. 10 and 12. We shall only give the results for the larger boundary ($r_{\max} = 40$ fm). The calculations have been performed as described in Ref. [20]. The independent-particle model gives a dipole cross section of 480 mb, whereas the three-body model gives 570 mb. The latter result is in fair agreement with the value deduced above, of the order of 600 mb. Since our three-body model does not yet have correlations in the final state we can anticipate that a full calculation would produce an even larger dipole cross section.

8. Conclusion

To study pairing in weakly bound nuclei, we proposed a three-body model Hamiltonian which can be solved over a large spatial domain using two-particle Green's functions. An important feature of the Hamiltonian is that the interaction

between valence nucleons be physically sensible in both the nuclear interior and in the far surface region. Within the constraints of a delta-function parameterization, we achieved this by making the interaction density dependent. At low density, our interaction reproduces the nearly bound virtual state of free nucleon scattering. Choosing the density dependence to fit the empirical pairing in the nuclei ^{14}C and ^{12}Be, we found that the interaction is reduced to nearly zero at nuclear matter density. This is in qualitative agreement with nuclear matter calculations in Brueckner theory [21].

The interaction between valence nucleons and the core is taken as a Woods–Saxon potential with parameters close to standard shell model values. Unfortunately, it is not possible to use a standard parameter set without any adjustment, because the pairing is very sensitive to the single-particle properties of the Hamiltonian when the levels are nearly unbound. Thus, the strength of the Woods–Saxon potential must be obtained by fitting the single-particle energies in each case separately.

The numerical method used to solve the Hamiltonian equation is by the two-particle Green's function technique in coordinate space. This method is only feasible for contact interactions (δ-functions), which is the reason we used this form of residual interaction. It permits accurate solution of the Hamiltonian equation even for cases in which the binding energy is of the order of 100 keV. Then the wave functions extend out to many tens of fermis, and coordinate space volumes with radii of the order of 50 fm are necessary to get fully converged results.

The two-particle binding energies we obtain with the density dependent contact interaction are in reasonable accord with the empirical data of the nearly unbound p-shell nuclei. Thus ^{10}He is predicted to be unbound, in agreement with experiment, and the weak binding energy of ^{11}Li is reproduced. We also examined the sd-shell nucleus ^{14}Be, which is bound by 1.3 MeV. The appropriate single-particle energies are not known in this case, but our Hamiltonian predicts binding for d-wave resonance energies as high as 3 MeV. However, in view of the approximations in our model, the good agreement for the ^{11}Li binding is somewhat fortuitous. We have ignored finite range effects in the interaction and set its stength to give an infinite scattering length. We have also ignored effects of core recoil[1] and core excitations, treating all core effects by the phenomenological density dependence of the interaction. The calibration of this interaction to reproduce the two-neutron binding in ^{12}Be and ^{14}C introduces some uncertainty, since our model is probably less reliable for more tightly bound nuclei. Some of these limitations, with respect to the free interaction and the core recoil, could be overcome using the Fadeev method, as for example in Ref. [22].

One of the theoretical interests in these weakly bound nuclei is the possibility to observe the very extended three-body bound states predicted by Efimov. According to Efimov's theory, the scattering lengths in the three-body problem set the size of

[1] Upon the advice of the referee, we estimated core recoil effects by replacing the mass m of a nucleon in the Hamiltonian by an effective mass of $m(A-2)/(A-1)$. With the other parameters recalculated to reproduce the physical constraints, we found the binding energy in ^{11}Li reduced from 200 to 100 keV.

the scale for the extension of the most weakly bound states. We found no evidence in our numerical study for an extra state state in ^{14}Be. However, with our numerical limitations we cannot rule it out as a possibility. But certainly in ^{11}Li the single-particle resonance energy is too high to support an additional state.

We examined the wave function of ^{11}Li in some detail, asking how well simplified models and pictures describe its form. An especially convenient model is the independent particle model using the Woods–Saxon potential and an adjusted separation energy. To describe the asymptotic behavior of the single-particle density, we found that the optimum separation energy is slightly greater than the physical two-particle separation energy. However, the radius of the adjusted potential should be somewhat larger than what the usual parameters give, so the r.m.s. radius of the single particle density is actually quite close to that obtained in the weak binding shell model, taking the standard shape of the Woods–Saxon potential but adjusting its depth to make the neutron separation energy equal the physical two-particle separation energy.

The two-particle density shows very strong correlations between the valence nucleons at large distances; the relative wave function follows the free-scattering wave function quite closely. Thus the *di*-neutron model, treating the ^{11}Li as a neutron pair of fixed internal structure, has at least qualitative validity.

We applied the model to the dipole excitation strength function, which is one of the interesting measured properties of ^{11}Li. In the calculation, we used the fully correlated ground state wave function but ignored correlations in the final state. This model predicts a rather large Coulomb breakup cross section, as was found experimentally. However, the interaction should be included in the final state, which is probably feasible within the present calculational framework. This improvement would provide a credible model to describe the correlations between final state neutrons in Coulomb fragmentation which can also be studied experimentally.

APPENDIX A: TWO-PARTICLE WAVE FUNCTIONS

The two-particle wave functions used to calculate the ground state and the dipole response of the correlated pair are constructed by coupling two single-particle wave functions to a total angular momentum of J, with $J=0$ and $J=1$, respectively. We shall discuss these two cases separately in the following.

Ground State, $J=0$

The ground state of the correlated pair has angular momentum $J=0$ and positive parity. The l and j quantum numbers of the two shell model states must therefore be identical, whereas the radial quantum numbes (n, n') can be different. Our j-coupled single-particle states follow the usual phase convention,

$$\psi_{nljm}(\mathbf{r}) = \phi_{nlj}(r) \sum_{m_l, m_s} (lm_l \tfrac{1}{2} m_s \mid jm)\, Y_{lm_l}(\hat{r})\, \chi_{m_s}, \tag{A.1}$$

where ϕ_{nlj} is a radial wave function and χ_m is a spin function. The two-particle wave function is obtained by coupling to $J=0$,

$$\Psi^{(2)}_{nn'lj}(\mathbf{r}_1, \mathbf{r}_2) = \sum_m (jmj-m \mid 00)\, \psi_{nljm}(\mathbf{r}_1)\, \psi_{n'lj-m}(\mathbf{r}_2). \tag{A.2}$$

This wave function is not antisymmetric if $n \neq n'$. We will return to this point later on.

Equations (A.1)–(A.2) are not the most convenient to calculate the wave function. A simpler formula can be obtained by evaluating (A.1)–(A.2) in a reference frame in which the z-axis points in the direction of $\hat{r}_1$. Then

$$Y_{l,m_{l1}}(\hat{r}_1 = \hat{z}) = \sqrt{(2l+1)/4\pi}\, \delta_{m_{l1},0}. \tag{A.3}$$

Inserting this into (A.1), with $m = m_1$ and $m_{l2} = -(m_1 + m_2)$, we obtain

$$\Psi^{(2)}_{nn'lj}(\mathbf{r}_1, \mathbf{r}_2) = \frac{\phi_{nlj}(r_1)\, \phi_{n'lj}(r_2)}{\sqrt{4\pi}} \sum_{m_1, m_2} \chi^{(1)}_{m_1} \chi^{(2)}_{m_2} C^{lj}_{m_1 m_2} Y_{l,m_{l2}}(\theta_{21}), \tag{A.4}$$

where θ_{21} is the angle between the two position vectors. The C coefficients in (A.4) are given by

$$C^{lj}_{m_1 m_2} = \sqrt{2l+1}(jm_1\, j-m_1 \mid 00)(l0\tfrac{1}{2}m_1 \mid jm_1)(l-(m_1+m_2)\tfrac{1}{2}m_2 \mid j-m_1). \tag{A.5}$$

One can show that the latter expression is

$$C^{lj}_{m_1, m_2} = \frac{(-1)^{l+1/2+m_2}}{2} \sqrt{\frac{2j+1}{2l+1}}, \tag{A.6a}$$

if $m_1 + m_2 = 0$, and if $m_1 + m_2 = \pm 1$ it is

$$C^{lj}_{m_1, m_2} = \frac{-(-1)^{j+m_2}}{2} \sqrt{2 - \frac{2j+1}{2l+1}}. \tag{A.6b}$$

We shall also need the two-particle wave functions at $\mathbf{r} = \mathbf{r}_1 = \mathbf{r}_2$ to compute the effect of the zero-range residual interaction. This part of the wave function turns out to be much simpler. Thus inserting $\hat{r}_2 = \hat{z}$ in Eq. (A.4), and using the relation (A.3) for the spherical harmonics and (A.6a) for the C coefficient, leads to the result,

$$\Psi^{(2)}_{nn'lj}(\mathbf{r}) = \frac{\phi_{nlj}(r)\, \phi_{n'lj}(r)}{\sqrt{4\pi}} (-1)^l \sqrt{\frac{2j+1}{8\pi}} \frac{1}{\sqrt{2}} (\chi^{(1)}_{1/2}\chi^{(2)}_{-1/2} - \chi^{(1)}_{-1/2}\chi^{(2)}_{1/2}). \tag{A.7}$$

The spin part is seen to be an $S=0$ state. This is typical when $\mathbf{r}_1 = \mathbf{r}_2$. The two-particle wave function does contain an $S=1$ component when $\mathbf{r}_1 \neq \mathbf{r}_2$. In that case the angular dependence provides an antisymmetry between the two particles. In order to achieve a fully antisymmetric wave function we would therefore only have to

symmetrize the radial part of the wave function. This is automatically taken care of if we include both combinations of wave functions in our space of two-particle states.

Excited States, $J \neq 0$

The two-particle shell model states used to calculate excited states of the pair can be constructed the same way as done above for $J=0$. Here we shall use a different and more elegant method to calculate the local (i.e., $\mathbf{r}_1 = \mathbf{r}_2$) two-particle wave functions. It is based on the helicity representation in which the angular and spin-dependent part of the single-particle states are given by (cf. Chap. 3A-1 of Ref. [7]),

$$|ljm\rangle = \sqrt{\frac{2j+1}{8\pi}} \sum_h \alpha(ljh)\, D^j_{mh}(\hat{r})\, \chi_h. \tag{A.8}$$

Here $\alpha(ljh) = (-1)^{(h+1/2)(j-l-1/2)}$ is a phase factor and h is the helicity, i.e., the spin projection on the direction of $\hat{r}$. It is simple to couple such two states to a total angular momentum state (JM),

$$|JM\rangle = \sum_{m_1 m_2} (j_1 m_1 j_2 m_2 \mid JM)\, |l_1 j_1 m_1\rangle\, |l_2 j_2 m_2\rangle. \tag{A.9}$$

One can use a well-known sum rule for D-functions, which holds when $\hat{r}_1 = \hat{r}_2$(see Ref. [7, Eq. (1A-43)]). One can then project the result on total helicity H, and obtain

$$\begin{aligned} |JMH\rangle = {} & \frac{\sqrt{(2j_1+1)(2j_2+1)}}{8\pi} \sum_{h_1 h_2} (j_1 h_1 j_2 h_2 \mid JH)\, D^J_{MH}(\hat{r}) \\ & \times \alpha_1(h_1)\, \alpha_2(h_2)\, \chi^{(1)}_{h_1} \chi^{(2)}_{h_2}. \end{aligned} \tag{A.10}$$

The total two-particle state has to be antisymmetric. This can only be achieved by requiring that the spin part is antisymmetric, since the coordinate part is automatically symmetric when the positions of the particles are identical. This implies that the total helicity H has to be zero. It is now easy to work out the result. Multiplying by the radial part of the wave function we obtain

$$\begin{aligned} \Psi^{(2)}_{JM}(\mathbf{r}) = {} & \phi_{n_1 l_1 j_1}(r)\, \phi_{n_2 l_2 j_2}(r)\, Y_{JM}(\hat{r})(-1)^{l_1} \sqrt{\frac{2j_1+1}{8\pi}} \left(j_1 \frac{1}{2} J0 \,\middle|\, j_2 \frac{1}{2} \right) \\ & \times \frac{1}{\sqrt{2}} (\chi^{(1)}_{1/2} \chi^{(2)}_{-1/2} - \chi^{(1)}_{-1/2} \chi^{(2)}_{1/2}). \end{aligned} \tag{A.11}$$

We note that this result is identical to (A.6) for $J=0$.

APPENDIX B: HAMILTONIAN DIAGONALIZATION

The ground state of the correlated pair can be found by diagonalizing the Hamiltonian (3.1). This is rather straightforward for a zero range interaction since the calculation of the matrix elements only involve the two-particle shell model wave functions at identical positions, which are given in Eq. (A.7). Thus we obtain the following Hamiltonian matrix,

$$\begin{aligned}\langle n_1 n_1' l_1 j_1 | \, H \, | n_2 n_2' l_2 j_2 \rangle &= \delta(n_1 \, n_1' \, l_1 \, j_1 \, ; \, n_2 n_2' l_2 j_2)(\varepsilon_{n_1 l_1 j_1} + \varepsilon_{n_1' l_1 j_1}) + (-1)^{l_1 + l_2} \\ &\times \frac{\sqrt{(2j_1+1)(2j_2+1)}}{8\pi} \\ &\times \int dr \, r^2 \phi_{n_1 l_1 j_1}(r) \, \phi_{n_1' l_1 j_1}(r) \, v_{\text{eff}}(r) \, \phi_{n_2 l_2 j_2}(r) \, \phi_{n_2' l_2 j_2}(r). \end{aligned} \tag{B.1}$$

The radial single-particle wave functions are solved in a finite box, so the continuum is discrete. Moreover, the Hamiltonian matrix is diagonalized in a truncated space with

$$\varepsilon_{nlj} + \varepsilon_{n'lj} \leqslant E_c, \tag{B.2}$$

where we have chosen $E_c = 40$ MeV as discussed in Section 2.

The ground state wave function is given by the sum

$$\Psi_{g_s}(\mathbf{r}_1, \mathbf{r}_2) = \sum_{nn'lj} \alpha_{nn'lj} \Psi^{(2)}_{nn'lj}(\mathbf{r}_1, \mathbf{r}_2), \tag{B.3}$$

where $\alpha_{nn'lj}$ are elements of the (normalized) eigenvector of the Hamiltonian matrix, associated with the lowest eigenvalue. The general expression for the two-particle shell model wave functions is given in Appendix A, Eq. (A.4).

The Hamiltonian matrix (B.1) is symmetric in the radial quantum numbers n and n' of the two-particle wave functions. The amplitudes α are therefore also symmetric in n and n'. One can in fact use this property to reduce the dimension of the diagonalization problem. Thus one could instead use a symmetrized set of two-particle wave functions,

$$\frac{\sqrt{2-\delta_{nn'}}}{2} (\Psi^{(2)}_{nn'lj}(\mathbf{r}_1, \mathbf{r}_2) + \Psi^{(2)}_{n'nlj}(\mathbf{r}_1, \mathbf{r}_2)), \tag{B.4}$$

and only include states with $n' \leqslant n$. This has been done in the numerical calculations but we shall not do it here since the notation becomes more cumbersome. We note, however, that this wave function is antisymmetric with respect to an interchange of the two particles, as discussed in Appendix A.

We shall now give the expressions for the one- and two-particle densities in the

ground state. The wave function (B.3) has four components, associated with the different orientations of the particle spins (m_1, m_2),

$$\Psi_{gs} = \frac{1}{\sqrt{4\pi}} \sum_{m_1 m_2} \Psi^{gs}_{m_1 m_2} \chi^{(1)}_{m_1} \chi^{(2)}_{m_2}. \tag{B.5}$$

The expression for $\Psi^{gs}_{m_1 m_2}$ can be obtained from Eqs. (A.4), and it can be written in the following way,

$$\Psi^{gs}_{m_1 m_2} = \sum_{lj} C^{lj}_{m_1 m_2} Y_{l,-(m_1+m_2)}(\hat{r}_2) \sum_{nn'} \alpha_{nn'lj} \phi_{nlj}(r_1)\, \phi_{n'lj}(r_2). \tag{B.6}$$

The coefficients $C^{lj}_{m_1 m_2}$ are given in Eqs. (A.6a)–(A.6b). We note that

$$\Psi^{gs}_{-m_1 -m_2} = -(\Psi^{gs}_{m_1 m_2})^*. \tag{B.7}$$

The two-particle density obtained from (B.5) is, therefore,

$$\rho_2(\mathbf{r}_1, \mathbf{r}_2) = \frac{2}{4\pi} (|\Psi^{gs}_{1/2\,-1/2}|^2 + |\Psi^{gs}_{1/2\,1/2}|^2). \tag{B.8}$$

This density depends on three variables, which are r_1, r_2 and the angle θ_{21} between $\mathbf{r}_1$ and $\mathbf{r}_2$, since we have chosen the z-axis to be identical to the direction of $\mathbf{r}_1$ in Appendix A. The two terms in (B.8) are the $S=0$ and the $S=1$ components, respectively, of the ground state density.

The single-particle density is easily obtained by integrating over the coordinates of one of the particles. From (B.6) and (B.8), and using the explicit expressions (A.6a) and (A.6b) for the C coefficients, one obtains

$$\rho_1(\mathbf{r}) = \frac{1}{4\pi} \sum_{lj} \sum_{nn'm} \alpha_{nn'lj} \alpha_{mn'lj} \phi_{nlj}(r)\, \phi_{mlj}(r). \tag{B.9}$$

We shall not give the expressions for the $S=0$ and the $S=1$ compónents of the single-particle density. They are more complicated since they involve overlap integrals of states with different j quantum numbers.

Finally, integrating over $\mathbf{r}$ we obtain the normalization

$$\int d\mathbf{r}\, \rho_1(\mathbf{r}) = \sum_{ljnn'} |\alpha_{nn'lj}|^2 = 1. \tag{B.10}$$

APPENDIX C: PAIRING FOR SEPARABLE FIELDS

It is very useful to have a simple way to test the numerical pairing calculations based on the two-particle Green's function method. One example is the case where the pairing matrix elements are separable. We shall here consider this example in

detail and illustrate it for a harmonic oscillator, single-particle potential combined with a density-independent, zero range pairing field. The correlated wave function is a solution to the integral equation

$$\Psi(\mathbf{r}_1, \mathbf{r}_2) = -\int d\mathbf{r}_1' \, d\mathbf{r}_2' G_2^{(0)}(E, \mathbf{r}_1, \mathbf{r}_2, \mathbf{r}_1', \mathbf{r}_2') \, v_{\text{eff}}(\mathbf{r}_1', \mathbf{r}_2') \, \Psi(\mathbf{r}_1', \mathbf{r}_2'), \tag{C.1}$$

where v_{eff} is the residual pairing interaction and $G_2^{(0)}$ is the independent, two-particle Green's function defined in Eq. (3.2). The solution to this equation requires in addition a determination of the energy eigenvalue E_α, which enters as the energy variable in the Green's function. Let us assume that the matrix elements of the pairing interaction are separable,

$$\langle \psi_{p_1} \psi_{p_2} | \, v_{\text{eff}} \, | \psi_{p_1'} \psi_{p_2'} \rangle = v_0 C_{p_1 p_2} C_{p_1' p_2'}. \tag{C.2}$$

The solution to the integral equation can be written as an expansion on two-particle wave functions,

$$\Psi = \sum_{p_1 p_2} \beta_{p_1 p_2} \psi_{p_1} \psi_{p_2}, \tag{C.3}$$

Insering this expression into Eq. (C.1) and making use of the separable form (C.2) leads to the equation

$$\beta_{p_1 p_2} = -\frac{v_0 C_{p_1 p_2}}{\varepsilon_{p_1} + \varepsilon_{p_2} - E} \sum_{p_1' p_2'} C_{p_1' p_2'} \beta_{p_1' p_2'}. \tag{C.4}$$

This equation is obviously fulfilled if we choose

$$\beta_{p_1 p_2} = \frac{C_{p_1 p_2}}{\varepsilon_{p_1} + \varepsilon_{p_2} - E}, \tag{C.5}$$

and require that the energy, $E = E_\alpha$, is determined by the dispersion relation

$$1 + \sum_{p_1 p_2} \frac{v_0 (C_{p_1 p_2})^2}{\varepsilon_{p_1} + \varepsilon_{p_2} - E_\alpha} = 0. \tag{C.6}$$

The associated eigenfunctions (C.3) are then determined by the expansion coefficients (C.5) evaluated at $E = E_\alpha$.

We note that this procedure is similar to the pairing calculation for free particles performed in Section 2. We also note that it is exact when the single-particle potential is a harmonic potential (without spin-orbit) and the pairing interaction is density-independent and of zero range. This follows from the fact that the motions of the two nucleons can be separated into a relative and a center of mass motion. The center of mass motion is unaffected by the pairing, and we can ignore it and

assume that it is in the ground state of the oscillator. The pairing matrix elements for the relative motion are

$$\langle \psi_n(\mathbf{r}) |\, v_0\, \delta(\mathbf{r})\, | \psi_{n'}(\mathbf{r}) \rangle = v_0 \psi_n(0)\, \psi_{n'}(0), \tag{C.7}$$

which has the separable from required in (C.2). We note that the matrix elements are non-zero only for s-states. The subscript n therefore indicates the radial quantum number of the s-state wave functions.

Using the well-known expressions for the harmonic oscillator wave functions it is now a simple numerical problem to solve the dispersion relation (C.6), with $C_{p_1 p_2} = \psi_n(0)$. This is done in a truncated oscillator basis which includes all s-states with $n \leqslant n_{\max}$. In order to test the numerical calculations based on the two-particle Green's function it is important to choose a truncation that is consistent with the cutoff in the two-particle energy spectrum, E_c. Thus the maximum radial quantum number for the relative motion, $n_{\max}$, should be determined by the condition

$$\tfrac{3}{2}\hbar\omega_0 + (\tfrac{3}{2} + 2n_{\max})\,\hbar\omega_0 \leqslant E_c. \tag{C.8}$$

Note that it is important to include the ground state energy for the center of mass motion in this relation, in order to make a consistent comparison to the results obtained from the two-particle Green's function method.

APPENDIX D: Dipole Matrix Elements

We display here the electric dipole matrix elements between the ground state of the pair and continuum excited states. Since a neutron has an effective dipole charge of $-Ze/A$, the dipole operator is

$$D_M(\mathbf{r}) = -\frac{Ze}{A}\, r Y_{1,M}(\hat{r}). \tag{D.1}$$

We first need the single-particle matrix elements of the dipole operator between bound and continuum states. The final state radial wave function, ϕ^c_{lj}, is normalized to one state per unit energy. This is formally written

$$\langle \phi^c(E) \mid \phi^c(E') \rangle = \delta(E - E'). \tag{D.3}$$

In practical terms, Eq. (D.3) requires that the continuum wave functions are normalized to the asymptotic form

$$\phi^c(r) \to \frac{\sin(kr + \delta)}{r} \sqrt{2m/\hbar^2 \pi k}, \tag{D.4}$$

where $k = \sqrt{2mE/\hbar^2}$ and δ is the phase shift. The single-particle matrix elements of

the dipole operator are conveniently expressed in terms of the standard reduced matrix element,

$$\langle j'm'|\, D_M\, |jm\rangle = \frac{(jm1M \mid j'm')}{\sqrt{2j'+1}}\, \langle cl'j'\|\, D\, \|nlj\rangle. \tag{D.5}$$

The formula for the reduced matrix element of the dipole operator is given by the formula

$$\langle cl'j'\|\, D\, \|nlj\rangle = -e\frac{Z}{A}(-)^{j'+1/2}\left(j\,\frac{1}{2}\,j'-\frac{1}{2}\,\middle|\,10\right)\sqrt{(2j+1)(2j'+1)/4\pi}$$

$$\int_0^\infty \phi^c_{l'j'}(r)\, r\phi_{nlj}(r) r^2\, dr, \qquad \text{if} \quad l+l' \text{ odd},$$

$$= 0, \qquad \text{if} \quad l-l' \text{ even}. \tag{D.6}$$

We are interested in the matrix element between two-particle states in which one of the states (the ground state) has components of the form $|nn'l(jj)^0\rangle$, where the single-particle wave functions have quantum numbers nlj and $n'lj$. The other state has the form $|(jj')^1_M\rangle$; the single-particle wave functions here are continuum states with energies e_1 and e_2 and orbital angular momenta l and l'. We first consider the operator $D(\mathbf{r}_2)$ which acts only on the second particle. Its two-particle matrix element is given by

$$\langle (jj')^1_M|\, D_M(\mathbf{r}_2)\, |nn'l(jj)^0\rangle = \langle \phi^c_{lj} \mid \phi_{nlj}\rangle \frac{\langle cl'j'\|\, D\, \|n'lj\rangle}{\sqrt{3(2j+1)}}. \tag{D.7}$$

To this must be added the matrix element of $D(\mathbf{r}_1)$. This is given by an identical expression except for the phase factor,

$$\langle (j'j)^1_M|\, D_M(\mathbf{r}_1)\, |nn'l(jj)^0\rangle$$

$$= (-1)^{j'-j+1}\langle \phi^c_{lj} \mid \phi_{n'lj}\rangle \frac{\langle cl'j'\|\, D\, \|nlj\rangle}{\sqrt{3(2j+1)}}. \tag{D.8}$$

The $B(E1,\uparrow)$ differential in the kinetic energy of the two emitted neutrons is related to the matrix elements, Eqs. (D.7)–(D.8), and to the ground state amplitudes $\alpha_{nn'lj}$ by the equation

$$\frac{d^2B(E1,\uparrow)}{de_1\, de_2} = 3\sum_{j_1 j_2}\left|\sum_{nn'lj}\alpha_{nn'lj}\langle (j_1 j_2)^1_M|\, D_M(\mathbf{r}_1) + D_M(\mathbf{r}_2)\, |nn'l(jj)^0\rangle\right|^2. \tag{D.9}$$

We used these expressions to calculate the differential $B(E1)$ strength shown in Section 7, Fig. 11.

ACKNOWLEDGMENTS

We are grateful to Dieter Kurath for valuable discussions. This work was supported by the National Science Foundation under Grant PHY 87-14432 and the U.S. Department of Energy, Nuclear Physics Division under Contract W-31-109-ENG-38.

REFERENCES

1. T. HOSHINO, H. SAGAWA, AND A. ARIMA, *Nucl. Phys. A* **506** (1990), 271.
2. R. REID, *Ann. Phys. (N.Y.)* **50** (1968), 411.
3. G. BERTSCH AND S. F. TSAI, *Phys. Rep. C* **18** (1975), 127.
4. C. THIBAULT *et al.*, *Phys. Rev. C* **12** (1975), 644.
5. J. M. WOUTERS *et al.*, *Z. Phys. A* **331** (1988), 229.
6. K. H. WILCOX *et al.*, *Phys. Lett. B* **59** (1975), 142.
7. A. BOHR AND B. R. MOTTELSON, "Nuclear Structure," Vol. I, Benjamin, New York, 1969.
8. A. H. WAPSTRA AND G. AUDI, *Nucl. Phys. A* **432** (1985), 55.
9. F. AJZENBERG-SELOVE, *Nucl. Phys. A* **449** (1986), 1; **506** (1990), 1.
10. S. COHEN AND D. KURATH, *Nucl. Phys. A* **73** (1965), 1.
11. F. AJZENBERG-SELOVE, *Nucl. Phys. A* **490** (1988), 1.
12. V. EFIMOV, *Nucl. Phys. A* **210** (1973), 157.
13. G. F. BERTSCH, B. A. BROWN, AND H. SAGAWA, *Phys. Rev. C* **39** (1989), 1154.
14. G. F. BERTSCH AND J. FOXWELL, *Phys. Rev. C* **41** (1990), 1300.
15. G. BERTSCH, H. ESBENSEN, AND A. SUSTICH, *Phys. Rev. C* **42** (1990), 758.
16. L. JOHANNSEN, A. S. JENSEN, AND P. G. HANSEN, *Phys. Lett. B* **244** (1990), 357.
17. H. KUCHAREK, P. RING, AND P. SCHUCK, *Z. Phys. A* **334** (1989), 119.
18. T. UCHIYAMA AND H. MORINAGA, *Z. Phys. A* **320** (1985), 273.
19. T. KOBAYASHI *et al.*, *Phys. Lett. B* **232** (1989), 51.
20. A. WINTHER AND K. ALDER, *Nucl. Phys. A* **319** (1979), 518.
21. J. W. CLARK AND C. H. YANG, *Lett. Nuovo Cimento* **2** (1971), 379.
22. J. BANG AND C. GIGNOUX, *Nucl. Phys. A* **313** (1979), 119.